Journal of Materials Chemistry A

Accepted Manuscript

ROYAL SOCIETY OF CHEMISTRY

www.rsc.org/materialsA

Cite this: DOI: 10.1039/c0xx00000x

www.rsc.org/xxxxxx

ARTICLE TYPE

Ultra high performance multi-element doped mesoporous carbon catalyst derived from poly(4-vinylpyridine)

Chenghang You[a], Dai Dang[a], Xiaochang Qiao[a], Guanghua Wang[a], Wenjun Fan[a], Rong Chen[a], Yingwei Li[a], Xiuhua Li[a], Shijun Liao[a]*

Received (in XXX, XXX) Xth XXXXXXXXX 20XX, Accepted Xth XXXXXXXXX 20XX
DOI: 10.1039/b000000x

A high performance doped carbon catalyst with ordered mesoporous structures and a high surface area (1217 m^2 g^{-1}) was prepared through a nanocasting-pyrolysis procedure by using poly(4-vinylpyridine) and iron chloride as the precursors and SBA-15 as the templates. The catalyst exhibited excellent oxygen reduction reaction (ORR) performance, which can be far more active than a commercial Pt/C catalyst in alkaline media, with its half-wave potential (-0.083 V, *vs.* Ag/AgCl) 64 mV more positive and the current density at -0.1 V (*vs.* Ag/AgCl, -3.651 mA cm^{-2}) almost three times higher than those of commercial Pt/C catalyst (-0.147 V, *vs.* Ag/AgCl, and -0.967 mA cm^{-2}), respectively. To our knowledge, it is one of the best carbon-based ORR catalysts to date in an alkaline medium. In addition to the outstanding ORR performance, our catalyst also illustrated excellent stability, methanol tolerance, and high catalytic efficiency. It is found that the total N contents and the compositions of each N species in the catalysts strongly depend on the pyrolysis temperatures. Furthermore, we found that the SBA-15 templates not only give catalyst well-defined mesoporous structures, but also seem to help increase the total N content whilst the proportion of each N species in the catalyst is not changed obviously.

Introduction

Due to their high electrocatalytic performance toward oxygen reduction reaction (ORR), low cost, and potential to replace traditional Pt-based electrocatalysts in novel electrochemical energy systems[1-6], such as proton exchange membrane fuel cells (PEMFCs)[7-11], direct methanol fuel cells (DMFCs)[12, 13], and metal-air batteries[14-17], carbon-based ORR catalysts, especially nitrogen-doped carbons, have become one of the most attractive topics in new energy fields in recent years[18-20]. During the past several years, numerous efforts have been paid in this area and great progress has been made. However, there is still a long way to go before these catalysts are available in practical applications, with one key issue being that their ORR electrocatalytic performance and stability remain limited. Thus, exploring carbons with better ORR performance and stability is still of great importance for the commercialization of those advanced energy systems.

For N-doped carbons, graphitic and pyridinic N species have recently been confirmed to play the most important role among all the N species in the catalysts during the ORR process[21-24]. Thus, appropriately increasing the amounts (or modifying the compositions) of these two active N species will possibly result in an enhanced ORR performance. Compared with graphitic N species, which can only be incorporated into carbons during the uncontrollable annealing process at high temperatures, pyridinic N species can be more easily introduced into precursors via compounds containing pyridine rings. During the pyrolysis procedures at high temperatures, pyridinic N species can be efficiently transformed into graphitic N species[25], which offers a potential and facile way to tune the compositions of these two active N species by simply controlling the pyrolysis temperatures.

In addition, it is also well known that pyridine rings can complex transient metals ions, such as Fe^{3+}, Co^{2+}, etc., to form desirable M-N_x microstructures (M = Fe, Co, etc., and typically x = 2, 4, 6)[26-29] due to the lone pair electrons of N atoms. This complexion effect cannot only help the homogeneous dispersion of these metals but also enable us to modify precursors' structures at molecular level, which will be helpful for tuning the interaction among the components and enhancing both the activity and durability of the final catalysts[30]. Herein, it will be convincible that a metal-based high pyridine containing polymer, which possesses all the features mentioned above, can be the very precursor for a desirable high performance carbon-based ORR catalyst.

In addition to fabricating potential active sites, giving catalysts suitable porous structures, especially mesoporous structures, can be another effective way to achieve enhanced ORR performance[28, 31-34], which are believed to be crucial for easing mass transfer, providing high surface areas, and increasing the number of exposed active sites[31, 35-37].

So far as we know, using metal-based high pyridine content polymer as a versatile precursor to prepare ordered mesoporous carbon-based ORR catalysts is still rarely reported.

Inspired by these factors, we developed a novel high performance doped carbon catalyst, with ordered mesoporous structures, high surface area (1217 m^2g^{-1}), through a nanocasting-

pyrolysis method by using ferric chloride ($FeCl_3$) and poly(4-vinylpyridin) as the precursors and SBA-15 as the templates. Excitingly, the catalyst exhibited excellent ORR performance, which can be far more active than that of a commercial Pt/C catalyst, with its half-wave potential (-0.083 V, *vs.* Ag/AgCl) 64 mV more positive and current density at -0.1 V (*vs.* Ag/AgCl, -3.651 mA cm^{-2}) almost three times higher than those of commercial Pt/C catalyst (-0.147 V, *vs.* Ag/AgCl, and -0.967 mA cm^{-2}), respectively. To our knowledge, it is one of the best carbon-based ORR catalysts to date in an alkaline medium. In addition to the outstanding ORR performance, our catalyst also illustrated excellent stability, methanol tolerance, and high catalytic efficiency. By changing the pyrolysis temperatures, we tuned the total N contents and the compositions of each N species in the resulting catalysts, and found that the total N content and the composition of each N species did play important roles in enhancing catalysts' ORR performance. By comparing the catalysts derived from precursors containing different amounts of SBA-15, we found that the added SBA-15 cannot only provide catalyst with well-defined ordered mesoporous structures but also seem helpful for maintaining catalyst's total N content without significantly changing the proportion of each N species during the pyrolysis procedure.

Experimental

Preparation of catalysts

The typical preparation of catalysts is as followed: briefly, 3.2 g 4-vinylpyridine (4-VP) was first polymerized in 100 mL N, N'-dimethylformamide (DMF) at 70 ^oC in a N_2 atmosphere by using trace amount of azodiisobutyronitrile (AIBN) as the initiator. After the polymerization was completed, 1 g SBA-15 and another 100 mL DMF containing 0.81 g $FeCl_3$ was added (the mole ratio of 4-VP monomer and $FeCl_3$ was approximately 6:1). The mixture was then refluxed for 12 h before it was evaporated at 110 ^oC. The obtained composite powder was then programmatically heated and pyrolyzed at 900 ^oC for 1 h in an Ar flow, followed by leaching in a hydrofluoric acid solution to remove the SBA-15 templates. The obtained catalyst was then denoted as CPVFe-S-900, in which "S" represents the SBA-15 and "900" refers to the annealing temperature applied. By using similar procedures, some other catalysts were obtained, without SBA-15 in the precursor or prepared under various pyrolysis temperatures. These catalysts were then named CPVFe-900, CPVFe-S-600, and CPVFe-S-750, respectively.

Preparation of working electrodes

We used a glassy carbon electrode (GCE, with a diameter of 5 mm and an electrode area of 0.1964 cm^2) as the working electrode substrate. Before every measurement, the GCE surface was cleaned in ethanol under ultrasonication, followed by polishing with α-Al_2O_3 slurry (50 nm) on a microcloth, rinsing with deionized (DI) water and drying under an infrared lamp.

The slurry of catalysts was prepared by mixing 5.0 mg catalyst and 1 mL ethanol solution of Nafion (0.25 wt%) under ultrasonication. And then, 20 μL slurry was pipetted onto the GCE surface, followed by drying under an infrared lamp. The catalyst loading was calculated to be 0.5 mg cm^{-2}.

Characterization

Scanning electron microscopy (SEM) images were recorded on a Nova Nano 430 field emission scanning electron microscope (FEI, Netherlands), with an acceleration voltage of 10 kV. Transmission electron microscopy (TEM) was operated on a JEM-2100 transmission electron microscope (JEOL, Japan) at an acceleration voltage of 200 kV. X-ray diffraction (XRD) was performed on a TD-3500 powder diffractometer (Tongda, China) at a scan rate of 0.5 ^{o} min^{-1}. X-ray photoelectron spectroscopy (XPS) was conducted on an ESCALAB 250 X-ray photoelectron spectrometer (Thermo-VG Scientific, USA). Specific surface areas and pore size distribution were measured by Brunauer-Emmett-Teller (BET) nitrogen adsorption-desorption at 77 K on a Tristar II 3020 gas adsorption analyzer (Micromeritics, USA). Thermogravimetrc analysis (TGA) curves were obtained by using a SDT Q600 simultaneous thermal analyzer (TA Instruments, USA) under a N_2 flow at a heating rate of 10 ^oC min^{-1}. The Fe residues in the final catalysts were measured by using inductively coupled plasma-atomic emission spectrometry (ICP-AES) with a Prodigy ICP-AES system (Leeman Labs Inc., USA). The Elemental Analysis (EA) of the catalysts was conducted on a Vario EL Cube (Elementar, Germany).

Electrochemical measurements

Electrochemical measurements were performed at room temperature by using a standard three-electrode glass cell on an IviumStat electrochemical workstation (Ivium, Netherlands), coupled with a rotating disk electrode (RDE) system (Pine Research Instruments, USA). An Ag/AgCl/KCl (3 M) and a Pt wire were used as the reference electrode and the counter electrode, respectively. For simplicity, the Ag/AgCl/KCl (3M) reference electrode will be abbreviated as Ag/AgCl in this work.

Before every measurement, the 0.1 M KOH solution was saturated with pure N_2 (99.999%) or pure O_2 (99.999%) for at least 30 min. All the current densities were normalized to the geometric area of the GCE (0.1964 cm^2). The chronoamperometric responses were obtained at -0.3 V (*vs.* Ag/AgCl) in an O_2-saturated 0.1 M KOH solution. Linear sweep voltammetry (LSV) measurements were conducted at a scan rate of 5 mV s^{-1} under different rotation rates from 1600 to 3600 rpm.

The electron transfer number per oxygen molecule involved was first calculated based on the Koutecky-Levich (K-L) equations following:

$$J^{-1} = J_L^{-1} + J_K^{-1} = B^{-1}\omega^{-1/2} + J_K^{-1}$$

$$B = 0.62nFC_0D_0^{2/3}v^{-1/6}$$

$$J_K = nF\kappa C_0$$

in which J is the measured current density; J_K and J_L are the kinetic and diffusion limiting current densities, respectively; ω is the angular velocity of the disk ($\omega = 2\pi N$, N denotes the linear rotation rate); n is the electron transfer number involved in the reduction of one O_2 molecule; F is the Faraday constant (F = 96,485 C mol^{-1}), C_0 is the bulk concentration of O_2; D_0 is the diffusion coefficient of O_2 in the KOH electrolyte; v is the kinetic viscosity of the electrode; κ is the electron transfer rate constant; and n and J_K can be obtained from the slope and intercept of the K-L plots, respectively. By using the values: $C_0 = 1.2\times10^{-3}$ mol L^{-1}, $D_0 = 1.9\times10^{-5}$ cm^2 s^{-1}, and $v = 0.01$ cm^2 s^{-1}, the electron transfer number (n) is calculated.

For the Tafel plots, the kinetic current was calculated from the RDE data under 1600 rpm by using the following equation[38]:

$$I_k = | I_L I(I_L - I)^{-1} |$$

The rotating ring disk electrode (RRDE) measurements were conducted using a glassy carbon disk (Pine Research Instruments, USA) with a polycrystalline Pt ring which was biased at 0.5 V (*vs.* Ag/AgCl), at a rotation rate of 1600 rpm in a 0.1 M KOH solution. The H_2O_2 yield and the electron transfer number (n) per oxygen molecule were calculated based on the following equations[39]:

$$\eta = 200 I_r (N I_d + I_r)^{-1}$$
$$n = 4 I_d (I_d + I_r N^{-1})^{-1}$$

where I_r and I_d refer to the ring and disk currents, respectively, and N is the collection efficiency, which was confirmed to be 0.36 by the reduction of $K_3Fe(CN)_6$.

Results and discussions

Fig. 1a exhibits the TGA results of PVPy [poly(4-vinylpyridine)] and PVPyFe precursors [prepared from PVPy and $FeCl_3$, for preparation details, **see ESI**.]. It can be observed that PVPy precursor was completely decomposed when the temperature reached 600 °C. However, Fe^{3+} ions mixed PVPyFe precursor shows significantly enhanced thermal stability, implying that there exists some interaction between PVPy and Fe^{3+} ions, and we suggest that this interaction should be the complexation occurred between the Fe^{3+} ions and pyridinic N of the PVPy, which can make PVPy molecular bridged and crosslinked, resulting in the higher thermal stability. To confirm the complexation, we characterized the two precursors by using XPS measurements. From the high resolution N1s XPS spectra of the two precursors (Fig. 1b), one can observe that the binding energy of pyridinic N species shifted positively from 398.7 to 399.1 eV, implying that the electron density around N atom reduced after Fe^{3+} ions were introduced. This shift in binding energy, we suggest, should be attributed to the complex effect between pyridine rings and Fe^{3+} ions, in which the lone-pair electrons of N atom can fill into the empty orbits of Fe^{3+} ions.

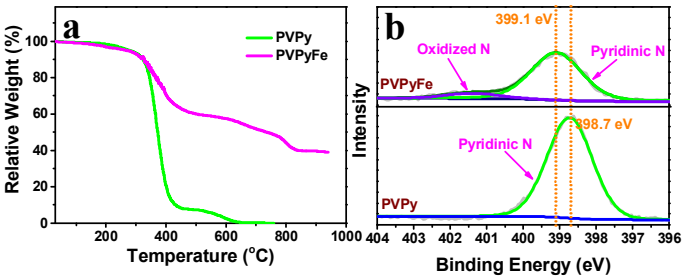

Fig. 1 (a) TGA curves of PVPy and PVPyFe; (b) High resolution N1s XPS spectra of the two precursors.

Fig. 2a-d demonstrate the SEM images of the as-prepared catalysts. From these images, one can observe that the catalyst CPVFe-900 has an irregular and bulky morphology, whereas the other three catalysts, casted by SBA-15 template, share nanorod-like morphologies. From the TEM images of CPVFe-S-900 (Fig. 2e, f), it can be observed that there are numerous well-defined ordered mesoporous structures in it, which can be also confirmed by the well-resolved diffraction peaks in its small-angle XRD patterns (Fig. S1). For the other two catalysts derived from the precursors containing SBA-15, similar well-define mesoporous structures can also be found in their TEM images and XRD patterns (Fig. S1 and S2), suggesting that these ordered mesoporous structures should originate from the SBA-15 templates.

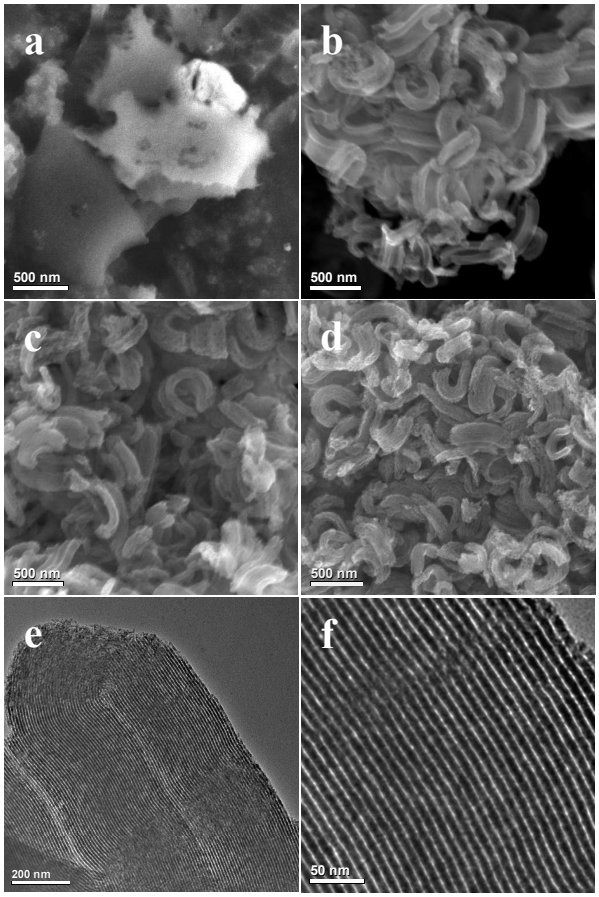

Fig. 2 SEM images of the as-prepared catalysts: (a) CPVFe-900; (b) CPVFe-S-600; (c) CPVFe-S-750; (d) CPVFe-S-900. (e) TEM image of CPVFe-S-900; (f) magnified TEM image of CPVFe-S-900.

Fig. 3a presents the N_2 adsorption-desorption isotherms of each catalyst. It can be found that the isotherms of the four catalysts are all type IV curves, with hysteresis loops in the medium- and high-pressure regions, indicating that there are abundant micro- and meso- porous structures in all of these obtained catalysts.

From the pore size distributions and cumulative volumes calculated from the N_2 adsorption-desorption results of the four catalysts (Fig. 3b and c), one can observe that the three catalysts casted by SBA-15 all have major pore densities around 5 nm, while the major pore density of CPVFe-900 (formed without any SBA-15 template) is much less than 5 nm.

From the accumulative volumes of CPVFe-900 and CPVFe-S-900 (Fig. 3c), it can be found that the volumes of micropores of the two catalysts prepared under the same temperature are similar (around 0.2 cm^3g^{-1}), while the volume of mesopores of CPVFe-S-900 is much higher than that of CPVFe-900. It is clear that the introduction of SBA-15 results in the formation of mesoporous structures of the catalyst.

For the catalysts prepared under different temperatures,

CPVFe-S-600, CPVFe-S-750, and CPVFe-S-900, it can be found that the pore volume of CPVFe-S-900 is by far the highest among the three catalysts (Fig. 3c), which, we suggest, should be attributed to the decomposition of unstable structures during the pyrolysis process.

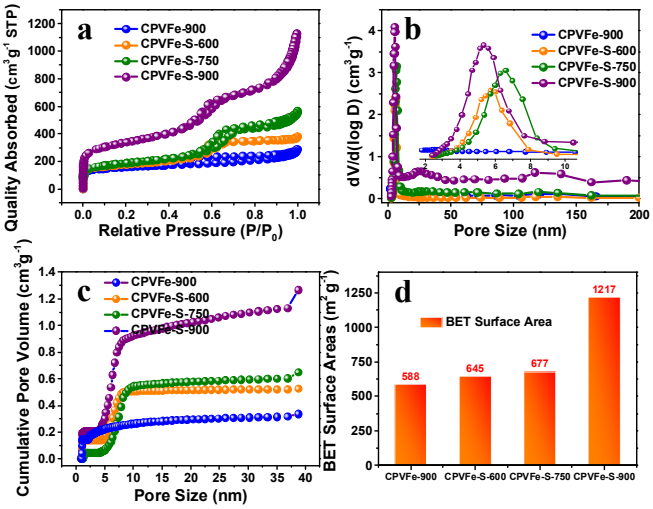

Fig. 3 (a) N_2 adsorption-desorption isotherms of the four as-prepared catalysts. (b) Pore size distribution calculated by using Barrett-Joyner-Halenda (BJH) analysis; the inserted figure shows the magnified pore density around 5 nm. (c) Cumulative pore volume of the four catalysts. (d) BET surface area of each catalyst.

With respect to the BET surface areas (Fig. 3d), CPVFe-S-900 has the highest surface area of 1217 $m^2 g^{-1}$, while CPVFe-900 has the lowest of 588 $m^2 g^{-1}$, (compared with 645 and 677 $m^2 g^{-1}$ for CPVFe-S-600 and CPVFe-S-750, respectively). The higher surface areas of catalysts derived from SBA-15 containing precursors suggest that the SBA-15 cannot only provide catalysts with well-defined, ordered, mesoporous structures but also increase catalysts' surface areas.

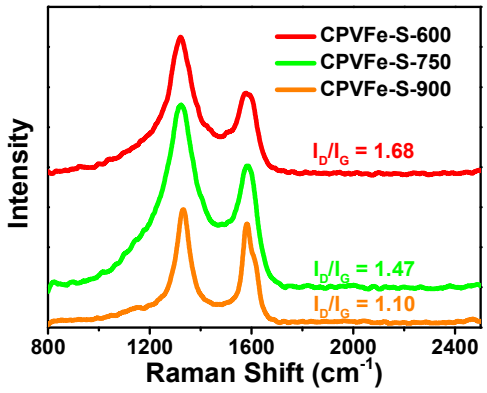

Fig. 4 Raman spectra for CPVFe-S-600, CPVFe-S-750 and CPVFe-S-900.

Fig. 4 shows the Raman spectra of various catalysts. It can be found that the I_D/I_G values decrease from 1.68 to 1.10 as the pyrolysis temperature rises, indicating that the graphiization degrees of the catalysts increase along with the temperatures and CPVFe-S-900 has the highest graphitization degree among the three catalysts.

Table 1 and S1 demonstrate the composition of the four catalysts, obtained from the XPS spectra (Fig. 5a) and EA, respectively. Obviously, CPVFe-S-900 has a much higher N content than CPVFe-900 does, which should be a proportional result of the confinement effect of the SBA-15 template.

As shown in Table 1, the N content of the SBA-15 templated catalysts decreased significantly with the pyrolysis temperature rising from 600 to 900 °C, indicating the decomposition of N composed structures of the catalyst at higher temperature.

With respect to Fe residues, which have recently been confirmed to be important for ORR performance[40], it can be found that the Fe contents in the four catalysts are rather close (Table 1), and CPVFe-S-900 has the lowest amount of 1.75 wt% (Fig. S3).

It should be also noted that the oxygen contents of SBA-15 templated catalysts are almost three times of that of CPVFe-900 without SBA-15 template. Considering the existence of Si residue in all the catalysts derived from precursors containing SBA-15 (Table 1), the high oxygen contents in these catalysts, we suggest, should originate from the SBA-15 residual, since it is difficult to remove the template completely by hydrofluoric acid treatment.

Table 1. Surface compositions of the as-prepared catalysts[a]

Catalyst	C (at%)	N (at%)	O (at%)	Fe (at%)	Si (at%)
CPVFe-900	96.86	0.77	1.82	0.54	-
CPVFe-S-600	85.56	8.24	5.36	0.5	0.33
CPVFe-S-750	91.11	3.37	4.81	0.39	0.32
CPVFe-S-900	91.70	2.59	5.13	0.36	0.22

[a]Hydrogen haven't been taken into account for the calculations.

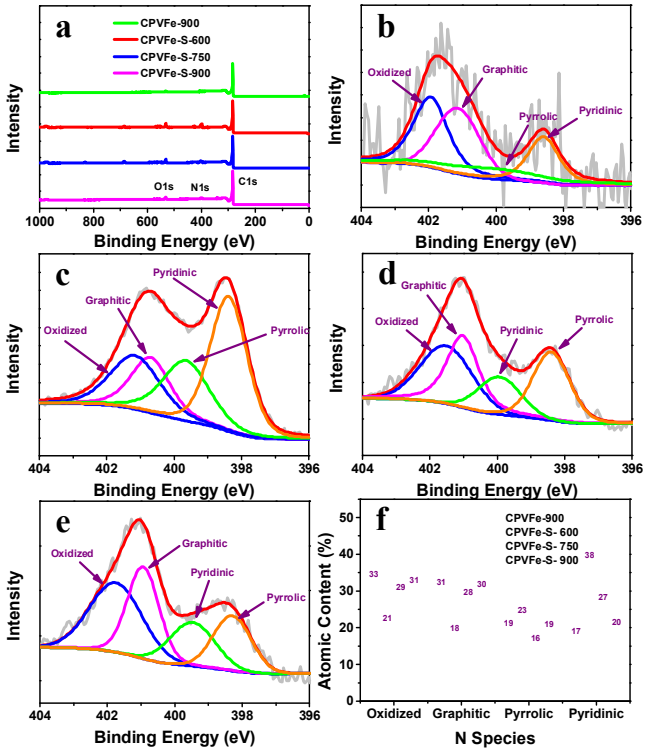

Fig. 5 (a) XPS spectra of the four obtained catalysts. N1s XPS spectra of (b) CPVFe-900, (c) CPVFe-S-600, (d) CPVFe-S-750, and (e) CPVFe-S-900. (f) Atomic ratio of each N species in the four catalysts.

From the N1s spectra and the deconvolution results of CPVFe-900 and CPVFe-S-900 (Fig. 5b, c and f), one can see that the atomic ratios for each N species in the two catalysts are quite similar, which might imply that the SBA-15 template can only increase the total N content but cannot significantly modify the proportion of each N species. For catalysts prepared under various pyrolyzing temperatures, it can be found that the N content in the catalyst decreases as the temperature rises (Table 1), which, we suggest, should be attributed to the decomposition of N containing structures at high temperatures.

Regarding the N species compositions in the three catalysts prepared under different annealing temperatures, it can be found that CPVFe-S-600 has the highest pyridinic N content (38 at%) but the lowest graphitic N content (18 at%), while CPVFe-S-900 has the lowest pyridinic N content (20 at%) but the highest graphitic N content (30%), compared with 27 and 29 at% for CPVFe-S-750, respectively, which can be the expected results of the transformation of pyridinic N into graphitic N during the pyrolysis procedure, suggesting that the N species composition in the final catalyst can be effectively modified by simply tuning the pyrolysis temperatures.

Based on the characterization results, it will be obvious that the introduction of SBA-15 in the precursor cannot only provide the catalysts with well-define, ordered, mesoporous structures but also increase the total N contents and the compositions of N species among the final catalysts. One can also expect that such differences in their compositions and structures will certainly result in various ORR performances.

Fig. 6a and b illustrate the LSV curves in 0.1 M KOH solution under an electrode rotation rate of 1600 rpm, the current density at -0.1 V (*vs.* Ag/AgCl) and the half-wave potentials of various catalysts. With the introduction of SBA-15 template, catalyst's performance was drastically enhanced. For CPVFe-S-900 catalyst, its half-wave potential is up to -0.083V, which is 200 mV higher than that of CPVFe-900 catalyst, and 83 mV higher than that of commercial Pt/C catalyst. As shown in Fig 5a and 5b, the ORR current density of the CPVFe-S-900 catalyst at -0.1 V (*vs.* Ag/AgCl) is up to 3.615 mA cm^{-2}, which is almost three times higher than that of commercial Pt/C catalyst (-0.957 mA cm^{-2}) , demonstrating the excellent ORR performance of our mesoporous catalyst prepared by nano-casting pyrolysis approach. To our knowledge, it is one of the best ORR catalysts in an alkaline medium to date.

What causes such a high ORR performance of CPVFe-S-900? From Fig. 5f, S3, and Table 1, we can see that CPVFe-900 and CPVFe-S-900 have the similar N species distribution (Fig. 5f) and almost the same Fe residue contents (Table 1 and Fig. S3). However, they have different total N contents (Table 1 and S1), porous structures (Fig. 2a, 2d, 3c) and surface areas (Fig. 3d). Compared with CPVFe-900 catalyst, we suggest that the high performance of CPVFe-S-900 should be attributed to the following aspects: (1) the high total N contents, as well as related high contents of active N species (including graphitic, pyridinic and pyrrolic N), which results in the high active site density for the catalyst; (2) the ordered porous structures and corresponding high surface area, which can supply smoother mass transfer and more exposed active sites.

Fig. 6c compares the contents of total N and each N species of CPVFe-900 and CPVFe-S-900 catalysts, and their catalytic activity towards ORR. It is true that the electrocatalytic activity increases with the total N content and active N content, indicating that the N content, especially the active N content, plays an important role for the performance of the catalyst. However, we also found that the activity of CPVFe-S-900 catalyst is almost 15 times as that of CPVFe-900, but its total N content and active N content are only 3.4 times of those of the CPVFe-900 catalyst, revealing that the significantly enhanced activity of CPVFe-S-900 catalyst is not only caused by the variation of N content or active N contents but also by other factors, which, we suggest, should be its ordered porous structures and corresponding high surface area.

Regarding the LSV curves of catalysts prepared at different pyrolysis temperatures, it can be found that catalysts' ORR performances were significantly affected by the pyrolysis temperatures. Among this series of catalysts, CPVFe-S-900 exhibited the highest electrocatalytic activity again.

For catalysts CPVFe-S-600 and CPVFe-S-900, as shown in Table 1, Fig. 5f and 6a, CPVFe-S-600 has a much higher N content than CPVFe-S-900 does. However, its ORR performance is poorer than that of CPVFe-S-900. Combining with the characterization results, we suggest that the lower activity of CPVFe-S-600 should be caused by its lower conductivity[22], resulting from the low graphitization of the materials (Fig. 4), and lower surface area (Fig. 3d) due to the lower pyrolysis temperature.

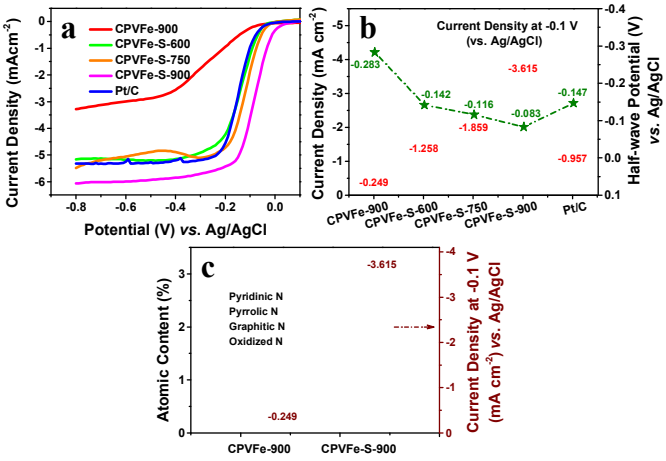

Fig. 6 (a) LSV curves of various catalysts in O_2-saturated 0.1 M KOH solution at a rotation rate of 1600 rpm. (b) half-wave potential and the current density at -0.1 V (*vs.* Ag/AgCl) of different catalysts from their LSV curves. (c) Atomic composition of each N species among all the surface atoms and the current density at -0.1 V (*vs.* Ag/AgCl) for CPVFe-900 and CPVFe-S-900.

Fig. 7a presents the Tafel plots of the four catalysts: 66.6, 71.5, 76.6, and 99.1 mV $decade^{-1}$ for CPVFe-S-900, CPVFe-S-750, CPVFe-S-600, and CPVFe-900, respectively. CPVFe-S-900 has the lowest Tafel slope, which also confirms its superior ORR performance and further indicates that it has the lowest overpotential among the four catalysts.

To understand the kinetics of the ORR occurring on our catalysts, we recorded their LSV curves in O_2-saturated 0.1 M KOH solution at different rotation rates (Fig. S5) and analyzed

these data by using the K-L equations (Fig. S6). Fig. 7b summarizes the electron transfer number calculated from the K-L equations in the potential range from -0.35 to -0.55 V (*vs.* Ag/AgCl). For CPVFe-900 and CPVFe-S-900, it can be found that, after introducing SBA-15 templates, catalyst's electron transfer number increased significantly. The electron transfer numbers of approximately four for CPVFe-S-600, CPVFe-S-750, and CPVFe-S-900 suggest that oxygen molecular can be almost directly reduced into OH^- by accepting four electrons without producing the intermediate OOH^-. Compared with the catalysts prepared using the SBA-15 template, CPVFe-900 has a much lower electron transfer number around 3, indicating that the ORR on this catalyst can only follow a pathway combining two-electron and four-electron processes. That is, the catalysts prepared using the SBA-15 templates have much higher catalytic efficiencies than the CPVFe-900 catalyst does.

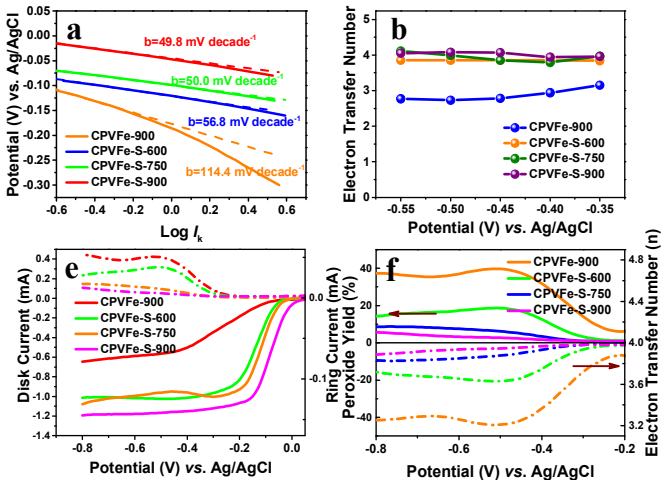

Fig. 7 (a) Tafel plots of various catalysts. (b) Electron transfer numbers obtained from the K-L analysis. (c) RRDE measurement results in 0.1 M KOH at a rotation rate of 1600 rpm. (d) Peroxide yields and electron transfer numbers of the catalysts (*vs.* potential) calculated from the RRDE measurement results.

To further confirm the ORR pathways on our catalysts, we conducted RRDE measurements and illustrated these results in Fig. 7c and d. It can be found that CPVFe-S-900 has the highest *n* value (above 3.9) and the lowest peroxide yield (between 2.0 and 5.5%) over the entire potential window ranging from -0.2 to -0.8 V (*vs.* Ag/AgCl), while CPVFe-900 has the lowest *n* value and the highest peroxide yield (between 10 and 40%) in the same potential window, which also suggests the highest catalytic efficiency of CPVFe-S-900 among the obtained catalysts, and is consistent with the results obtained from the K-L analysis.

Fig. 8 illustrates the current-time (i-t) chronoamperometric responses of CPVFe-S-900 and commercial Pt/C catalyst in an alkaline medium. As shown in Fig. 8a, CPVFe-S-900 has an outstanding methanol tolerance. When methanol was introduced, almost no changes was observed for CPVFe-S-900, while the ORR performance of commercial Pt/C dropped significantly upon the addition of methanol. Regarding the durability, it can be observed from Fig. 8b that CPVFe-S-900 exhibited outstanding stability. After 20,000 s continuous ORR at -0.3 V (*vs.* Ag/AgCl), CPVFe-S-900 maintained more than 97% of its initial ORR performance, whereas Pt/C electrode lost almost 20% of its initial performance under the same conditions.

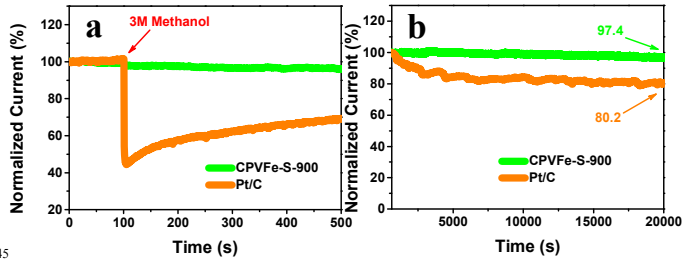

Fig. 8 (a) Current-time (i-t) chronoamperometric responses of CPVFe-S-900 and commercial Pt/C electrodes upon the introduction of 3 M methanol; (b) Current-time (i-t) chronoamperometric responses of CPVFe-S-900 and commercial Pt/C electrodes at -0.3 V (*vs.* Ag/AgCl) in O_2-saturated 0.1 M KOH at a rotation rate of 1600 rpm.

Conclusions

In this work, we developed a novel high-performance doped carbon catalyst, with ordered mesoporous structures and high surface area (1217 m^2g^{-1}), through a nanocasting-pyrolysis method by using poly(4-vinylpyridin) and $FeCl_3$ as the precursors and SBA-15 as the templates. Excitingly, the catalyst exhibited excellent ORR performance, which can be far more active than that of a commercial Pt/C catalyst, with a half-wave potential (-0.083 V, *vs.* Ag/AgCl) 64 mV more positive and a current density at -0.1V (*vs.* Ag/AgCl, -3.651 mA cm^{-2}) nearly three times higher than those of commercial Pt/C catalyst (-0.147 V, *vs.* Ag/AgCl, and -0.967 mA cm^{-2}), respectively. To our knowledge, it is one of the best carbon-based ORR catalysts in an alkaline medium to date. In addition to the outstanding ORR performance, our catalyst also illustrated excellent stability, methanol tolerance, and high catalytic efficiency. By changing the pyrolysis temperatures, we tuned the total N contents and the compositions of each N species in the resulting catalysts, and found that the various N contents and the compositions of each N species did play a vertical role in enhancing catalysts' ORR performance. By comparing the catalysts derived from precursors containing different amounts of SBA-15, we found that the added SBA-15 cannot only provided catalysts with well-defined, ordered, mesoporous structures but also seem helpful for maintaining the total N content without significantly changing the proportion of each N species during the pyrolysis procedure.

This catalyst's high ORR performance, outstanding stability and methanol tolerance, combining with its ordered mesoporous structures and high surface areas, will certainly make it promising for the practical applications in novel energy systems, such as PEMFCs, DMFCs, and metal-air batteries.

Acknowledgements

This work was supported by the National Science Foundation of China (NSFC Project Nos. 21276098, 21476088, 51302091, U1301245), Ministry of Science and Technology of China (Project No. 2012AA053402), Guangdong Natural Science Foundation (Project No.S2012020011061), and Department of Education of Guangdong Province (Project No. 2013CXZDA003).

Notes and references

[a]*The Key Laboratory of Fuel Cell Technology of Guangdong Province, School of Chemistry and Chemical Engineering, South China University of Technology, Guangzhou, 510641, China, Fax: +86 20 8711 3586. E-mail address: chsjliao@scut.edu.cn*

†Electronic Supplementary Information (ESI) available: additional experimental details, TEM images, small angle XRD diffraction patterns, linear voltammetric curves, and Koutecky–Levich plots, etc. See DOI: ‡

1. S. Gao, K. Geng, H. Liu, X. Wei, M. Zhang, P. Wang and J. Wang, *Energ Environ Sci*, 2015, **8**, 221-229.

2. W. Wei, H. W. Liang, K. Parvez, X. D. Zhuang, X. L. Feng and K. Mullen, *Angew Chem Int Edit*, 2014, **53**, 1570-1574.

3. J. Y. Cheon, J. H. Kim, J. H. Kim, K. C. Goddeti, J. Y. Park and S. H. Joo, *J Am Chem Soc*, 2014, **136**, 8875-8878.

4. J. Deng, P. J. Ren, D. H. Deng, L. Yu, F. Yang and X. H. Bao, *Energ Environ Sci*, 2014, **7**, 1919-1923.

5. Y. Hou, Z. Wen, S. Cui, S. Ci, S. Mao and J. Chen, *Adv Funct Mater*, 2015, **25**, 872-882.

6. P. Chen, L. K. Wang, G. Wang, M. R. Gao, J. Ge, W. J. Yuan, Y. H. Shen, A. J. Xie and S. H. Yu, *Energ Environ Sci*, 2014, **7**, 4095-4103.

7. C. H. You, X. Y. Zeng, X. C. Qiao, F. F. Liu, T. Shu, J. H. Zeng, L. Du and S. J. Liao, *Nanoscale*, 2015, **7**, 3780-3785.

8. C. H. You, S. J. Liao, X. C. Qiao, X. Y. Zeng, F. F. Liu, R. P. Zheng, H. Y. Song, J. H. Zeng and Y. W. Li, *J Mater Chem A*, 2014, **2**, 12240-12246.

9. C. You, S. Liao, H. Li, S. Hou, H. Peng, X. Zeng, F. Liu, R. Zheng, Z. Fu and Y. Li, *Carbon*, 2014, **69**, 294-301.

10. H. L. Peng, Z. Y. Mo, S. J. Liao, H. G. Liang, L. J. Yang, F. Luo, H. Y. Song, Y. L. Zhong and B. Q. Zhang, *Sci Rep-Uk*, 2013, **3**, 1765.

11. D. Deng, L. Yu, X. Chen, G. Wang, L. Jin, X. Pan, J. Deng, G. Sun and X. Bao, *Angew Chem Int Edit*, 2013, **52**, 371-375.

12. Y. Li, T. T. Li, M. Yao and S. Q. Liu, *J Mater Chem*, 2012, **22**, 10911-10917.

13. F. Su, J. Zeng, Y. Yu, L. Lv, J. Y. Lee and X. S. Zhao, *Carbon*, 2005, **43**, 2366-2373.

14. X. Zeng, C. You, L. Leng, D. Dang, X. Qiao, X. Li, Y. Li, S. Liao and R. R. Adzic, *J Mater Chem A*, 2015, **3**, 11224-11231.

15. X. Huang, H. Yu, H. Tan, J. Zhu, W. Zhang, C. Wang, J. Zhang, Y. Wang, Y. Lv, Z. Zeng, D. Liu, J. Ding, Q. Zhang, M. Srinivasan, P. M. Ajayan, H. H. Hng and Q. Yan, *Adv Funct Mater*, 2014, **24**, 6516-6523.

16. H. W. Park, D. U. Lee, P. Zamani, M. H. Seo, L. F. Nazar and Z. Chen, *Nano Energy*, 2014, **10**, 192-200.

17. D. U. Lee, J.-Y. Choi, K. Feng, H. W. Park and Z. Chen, *Adv Energ Mater*, 2013, **4**, 1301389.

18. C. G. Hu, L. X. Wang, Y. Zhao, M. H. Ye, Q. Chen, Z. H. Feng and L. T. Qu, *Nanoscale*, 2014, **6**, 8002-8009.

19. C. Han, X. Bo, Y. Zhang, M. Li, A. Nsabimana and L. Guo, *Nanoscale*, 2015, **7**, 5607-5611.

20. J. Wei, Y. Liang, X. Zhang, G. P. Simon, D. Zhao, J. Zhang, S. Jiang and H. Wang, *Nanoscale*, 2015, **7**, 6247-6254.

21. L. F. Lai, J. R. Potts, D. Zhan, L. Wang, C. K. Poh, C. H. Tang, H. Gong, Z. X. Shen, L. Y. Jianyi and R. S. Ruoff, *Energ Environ Sci*, 2012, **5**, 7936-7942.

22. W. Ding, Z. Wei, S. Chen, X. Qi, T. Yang, J. Hu, D. Wang, L. Wan, S. F. Alvi and L. Li, *Angew Chem Int Edit*, 2013, **125**, 11971-11975.

23. D. H. Deng, X. L. Pan, L. A. Yu, Y. Cui, Y. P. Jiang, J. Qi, W. X. Li, Q. A. Fu, X. C. Ma, Q. K. Xue, G. Q. Sun and X. H. Bao, *Chem Mater*, 2011, **23**, 1188-1193.

24. J. Chen, X. Wang, X. Cui, G. Yang and W. Zheng, *Chem Commun*, 2014, **50**, 557-559.

25. D. Usachov, A. Fedorov, O. Vilkov, B. Senkovskiy, V. K. Adamchuk, L. V. Yashina, A. A. Volykhov, M. Farjam, N. I. Verbitskiy, A. Grüneis, C. Laubschat and D. V. Vyalikh, *Nano letters*, 2014, **14**, 4982-4988.

26. Y. Zhu, B. Zhang, X. Liu, D. Wang and D. S. Su, *Angew Chem Int Edit*, 2014, **53**, 10673-10677.

27. H. Peng, S. Hou, D. Dang, B. Zhang, F. Liu, R. Zheng, F. Luo, H. Song, P. Huang and S. Liao, *Appl Catal B - Environ*, 2014, **158**, 60-69.

28. J. Y. Cheon, T. Kim, Y. Choi, H. Y. Jeong, M. G. Kim, Y. J. Sa, J. Kim, Z. Lee, T. H. Yang, K. Kwon, O. Terasaki, G. G. Park, R. R. Adzic and S. H. Joo, *Sci Rep-Uk*, 2013, **3**, 2715.

29. A. Kong, Y. Kong, X. Zhu, Z. Han and Y. Shan, *Carbon*, 2014, **78**, 49-59.

30. Z. Li, G. Li, L. Jiang, J. Li, G. Sun, C. Xia and F. Li, *Angew Chem Int Edit*, 2015, **54**, 1494-1498.

31. Y. Zheng, Y. Jiao, J. Chen, J. Liu, J. Liang, A. Du, W. M. Zhang, Z. H. Zhu, S. C. Smith, M. Jaroniec, G. Q. Lu and S. Z. Qiao, *J Am Chem Soc*, 2011, **133**, 20116-20119.

32. J. Liang, R. F. Zhou, X. M. Chen, Y. H. Tang and S. Z. Qiao, *Adv Mater*, 2014, **26**, 6074-6079.

33. J. Liang, Y. Zheng, J. Chen, J. Liu, D. Hulicova-Jurcakova, M. Jaroniec and S. Z. Qiao, *Angew Chem Int Edit*, 2012, **51**, 3892-3896.

34. T. Y. Ma, S. Dai, M. Jaroniec and S. Z. Qiao, *Angew Chem Int Edit*, 2014, **53**, 7281-7285.

35. Z. Liu, H. G. Nie, Z. Yang, J. Zhang, Z. P. Jin, Y. Q. Lu, Z. B. Xiao and S. M. Huang, *Nanoscale*, 2013, **5**, 3283-3288.

36. Y. G. Li, W. Zhou, H. L. Wang, L. M. Xie, Y. Y. Liang, F. Wei, J. C. Idrobo, S. J. Pennycook and H. J. Dai, *Nat Nanotechnol*, 2012, **7**, 394-400.

37. W. Kiciński, M. Szala and M. Bystrzejewski, *Carbon*, 2014, **68**, 1-32.

38. S. Mao, Z. Wen, T. Huang, Y. Hou and J. Chen, *Energ Environ Sci*, 2014, **7**, 609-616.

39. J. Wang, G. Wang, S. Miao, X. Jiang, J. Li and X. Bao, *Carbon*, 2014, **75**, 381-389.

40. L. Wang, A. Ambrosi and M. Pumera, *Angew Chem Int Edit*, 2013, **52**, 13818-13821.

Graphical Abstract

Ordered mesoporous carbon catalyst derived from iron-complexed poly(4-vinylpyridine), with a much higher ORR performance than a commercial Pt/C catalyst